

openKARST: A novel open-source flow simulator for karst systems

Jannes Kordilla^{a,*}, Marco Dentz^a and Juan J. Hidalgo^a

^a*Institute of Environmental Assessment and Water Research (IDAEA-CSIC), Groundwater and Hydrogeochemistry Group, Carrer de Jordi Girona 18-26, Barcelona, 08034, Spain*

ARTICLE INFO

Keywords:

Flow in karst conduit networks
Laminar and turbulent flows
Free-surface and pressurized flows

ABSTRACT

We introduce the open-source Python-based code openKARST for flow in karst conduit networks. Flow and transport in complex karst systems remain a challenging area of hydrogeological research due to the heterogeneous nature of conduit networks. Flow regimes in these systems are highly dynamic, with transitions from free-surface to fully pressurized and laminar to turbulent flow conditions with Reynolds numbers often exceeding one million. These transitions can occur simultaneously within a network, depending on conduit roughness properties and diameter distributions. openKARST solves the transient dynamic wave equation using an iterative scheme and is optimized with an efficient vectorized structure. Transitions from free-surface to pressurized flows in smooth and rough circular conduits are realized via a Preissmann slot approach in combination with an implementation of the Darcy-Weisbach and Manning equations to compute friction losses. To mitigate numerical fluctuations commonly encountered in the Colebrook-White equation, the dynamic switching from laminar to turbulent flows is modeled with a continuous Churchill formulation for the friction factor computation. openKARST supports common boundary conditions encountered in karst systems, as well as functionalities for network import, export and visualization. The code is verified via comparison against several analytical solutions and validated against a laboratory experiment. Finally, we demonstrate the application of the openKARST by simulating a synthetic recharge event in one of the largest explored karst networks, the Ox Bel Ha system in Mexico.


1. Introduction

Karst aquifers are a significant water resource worldwide and, in many regions such as the Mediterranean, an indispensable source for freshwater (Chen et al., 2017; Bresinsky et al., 2023). Given their importance for water resources management, addressing and mitigating environmental impacts and risks is crucial. In contrast to aquifer systems in unconsolidated porous materials, karst systems are characterized by their strong degree of fracturing both in the phreatic and vadose zone and conduit networks formed by dissolution processes, which are embedded in a porous-fractured matrix. Conduit networks are often residing in the hydraulically most dynamic parts, i.e. close to the groundwater table where the availability of dissolved carbon dioxide enhances the dissolution process of limestone. However, due to movements on geological time scales, dissolution horizons may also shift, such that conduit networks may either remain in the vadose zone under drained conditions or fully submerged below the groundwater table (Bakalowicz, 2015).

All compartments, that is, the surface zone, the vadose zone and the phreatic zone provide rapid flow pathways adjacent to a porous matrix (Kordilla et al., 2012; Shigorina et al., 2021), which leads to strong contrasts in hydraulic conductivity (Schmidt et al., 2014). Furthermore, despite their often thick vadose zones, karst aquifers are highly vulnerable to environmental impacts such as contamination from surface sources, rapid transmission of pollutants in conduit systems (Neuman, 2005), and changes in water quality and quantity due to shifts in land use and climate (Chen et al., 2018). Hence, this poses a challenge both for flow and transport modeling tools that must account for wide array of flow and transport processes on various time scales (Jourde and Wang, 2023).

Specifically flow within conduit networks sets karst system apart from many other hydrogeological systems. Conduits may reach diameters of several meters or more (Maqueda et al., 2023), at which point they may also be classified as caves. Due to their size, Reynolds numbers in conduits may exceed values of 1 million depending on pressure gradients. Starting from dry conditions, flows may occur as laminar free surface flows, shifting towards turbulent conditions as water depths increases (Reimann et al., 2011; Shoemaker et al., 2008). Once water levels

*Corresponding author

 jannes.kordilla@idaea.csic.es (J. Kordilla)
ORCID(s): 0000-0003-4083-4491 (J. Kordilla)

reach the conduit ceiling flows become pressurized. The representation of three-dimensional karst conduit systems and the simultaneous numerical solution of laminar, turbulent, free-surface and pressurized flow conditions on spatially heterogeneous conduit networks represents a fundamental challenge (Jourde and Wang, 2023).

Similar to the modeling of flow in fractured porous media (Berre et al., 2019), for karst media one can distinguish equivalent porous media (EPM) or single continuum approaches, dual continuum (DC) models, combined discrete continuum (CDC) models, and discrete conduit network (DCN) models (Kovács and Sauter, 2014; Hartmann et al., 2014; Jourde and Wang, 2023). The EPM approach (Scanlon et al., 2003) represents the hydraulically heterogeneous karst medium by an equivalent porous medium that is characterized by suitably defined averaged (upscaled) hydraulic properties (Larocque et al., 1999). The dual continuum approach models the karst as two linearly interacting continua with very different hydraulic properties that are representative of the porous matrix and conduit network (Cornaton and Perrochet, 2002; Kordilla et al., 2012). In the CDC approach, dominant conduits are explicitly modeled and embedded in a porous matrix (Kiraly, 1975). The CDC approach has been implemented in MODFLOW-CFP (Shoemaker et al., 2007) and MODFLOW-USG (Kresic and Panday, 2018). MODFLOW-CFP is an extended version of the MODFLOW groundwater modeling suite developed by the U.S. Geological Survey (USGS) written in Fortran with user interfaces for Windows. The versions, CFP Mode 1-3, cover (1) laminar flow using the Hagen-Poiseuille law, (2) turbulent flows via the Darcy-Weisbach equation and (3) both regimes and transitions. Furthermore, MODFLOW-CFP can handle dynamic interactions between conduits and the surrounding porous matrix. MODFLOW-CFP does not account for transient flow within conduits but models a (quasi) steady-state under the assumption that conduit flows reach a steady-state very quickly compared to the time scales within the remaining porous-matrix system. MODFLOW-USG (Panday et al., 2013) solves Darcy flow in the porous matrix using an unstructured grid, in which a connected linear network is embedded. The latter represents the network of dominant karst conduits. Flow options are pressurized laminar and turbulent flow as well as the diffusive wave equation for free-surface flow. DCN approaches represent the karst medium as a network of one-dimensional conduits (Jeannin, 2001) and disregard the impact of the porous matrix. Dynamic flow conditions in the connected network of conduits is quantified by the Saint Venant equations or dynamic wave model that accounts for laminar and turbulent flow under free surface and pressurized flow conditions. In this context, the Storm Water Management Model (SWMM, Rossman and Huber (2017) for flow in underground sewer systems has been used to simulate conduit drainage behavior in dominant connected karst structures (Campbell and Sullivan, 2002; Peterson and Wicks, 2006), and coupled to reservoir models to account for recharge, storage and transfer between compartments (Chen and Goldscheider, 2014).

The numerical modeling of dynamic free-surface and pressurized turbulent and laminar flow in karst networks is key for the assessment of flood events and draughts in the presence of rapid changes of the flow boundary conditions. Furthermore, new characterization methods and stochastic approaches for the simulation of karst network geometry and heterogeneity (Collon et al., 2017; Maqueda et al., 2023) require efficient tools for the modeling of dynamic flow conditions in large multiscale karst networks that enable to systematically quantify and upscale the impact of network geometry and heterogeneity on large scale flow behaviors. Thus, in this paper, we introduce a Python-based numerical platform to model complex transient flow dynamics in karst conduit networks.

The code allows for detailed simulations of flow in complex conduit networks employing a grid-free, graph-based numerical framework. This enables the simulation of fully transient dynamics of free surface and pressurized laminar and turbulent flows in highly complex karst network structures, for which currently no comprehensive open-source tool exists. Written in Python, the openKARST platform is aiming at a community-driven development process and follows an open-source philosophy. Due to the accessible Python environment and expandable code design, the openKARST platform can be easily adapted in the scientific community to ensure future developments with a focus on karst-specific processes, and conduit scale flow properties that reflect the impact of realistic conduit geometries in terms of roughness and geometry.

The paper is structured as follows. Section 2 presents the overall methodology. It states the network scale flow problem in terms of the continuity and momentum conservation equations that constitute the dynamic wave or Saint Venant equations. It discusses the space and time discretization of the flow equations including upstream weighting and inertial damping, and the iterative solution of the implicit non-linear system of equations by Picard iteration. Then it presents the geometrical and physical relations to close the resulting system of discrete equations, as well as boundary and initial conditions. Section 3 discusses the verification of the code in comparison to analytical solutions for steady-state free surface and pressurized flow, validation against experimental data, and an application example for flow in a real karst network geometry.

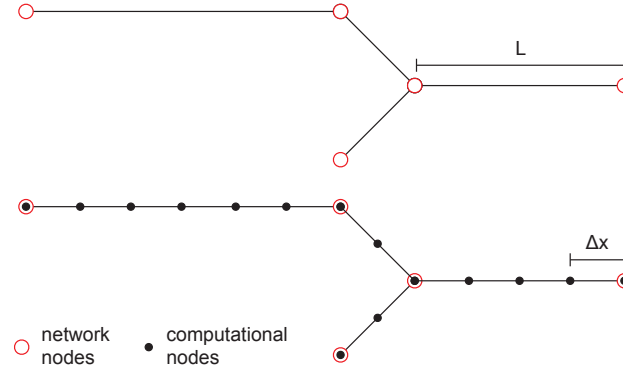


Figure 1: Spatial discretization of the underlying network showing both network nodes (red circles) and computational nodes (black dots). Note that the spacing Δx can be variable and different for each conduit of length L .

2. Methodology

We consider flow through a karst system that consists of a network of conduits as illustrated in Figure 1. Flow along single conduits is quantified by the Saint-Venant equations, which describe the average flow velocity or flow rate along the conduit. At the network nodes mass is conserved. In the following, we first summarize the Saint-Venant equations for flow along a single conduit and their implementation on the karst network. Then we describe the spatial and temporal discretization of the governing equations and their numerical solution.

2.1. Network flow

The karst system is represented as a network of N_o nodes and N_c conduits, see Figure 1. Each node is connected to d conduits, which defines the degree of the node. Conduits are characterized by the length L [L] and a constant hydraulic diameter $D = 4A/P$ [L], where A [L²] is the cross-sectional area and P [L] the perimeter of the conduit. We define the equivalent conduits radius by $R = D/2$. We consider transient free surface and pressurized flow, which is quantified by the flow rate or discharge Q [L³/T] and water depth y [L] along the conduit. From the water depth and the underlying conduit geometry one can determine the cross-sectional width of the free surface W , the discharge area $A \leq \mathcal{A}$, and the wetted perimeter P [L]. The wetted hydraulic radius and diameter are then given by $R = A/P$ [L] and $D = 4A/P$ [L]. Note that $D = 4R$ by definition. The average flow velocity along the conduit is given by $v = Q/A$ [L/T]. The areas and lengths characterizing the water phase along a conduit are functions of the water depth y only and can be determined based on the conduit shape. Conduits are represented as one-dimensional objects. The flow behavior is characterized by the flow rate Q and water depth y .

Mass is conserved in the system and the fluid density is constant. This means that at each node i the temporal change of the nodal volume V_i [L³] is equal to the net flow

$$\frac{dV_i}{dt} = \sum_{l=1}^{d_i} Q_{i,l} + Q_{i,r} \quad (1)$$

where $Q_{i,l}$ denotes the flow rate of conduit l at node i and $Q_{i,r}$ denotes the recharge or discharge flux at node i . In the following, the subscript i counts the nodes, the subscript l the conduits. Flow in a conduit l connecting the nodes i_1 and i_2 is determined by the Saint-Venant equations (Saint-Venant, 1871), which describe transient free surface flow through pipes or channels with variable geometry. They quantify the cross-sectionally averaged flow along conduits and are based on the following assumptions. (1) Small conduit slope: The slope of the conduit bottom is smaller than about 10% to minimize the influence of slope-induced acceleration. (2) Hydrostatic pressure distribution: The vertical acceleration of the flow is negligible, that is, the pressure distribution at any cross-section is hydrostatic. (3) Boundary friction: Friction at the boundary is modeled similar to steady-state flows, based on a constitutive relationship between flow velocity and shear stress. Under these assumptions, conservation of mass and momentum along the conduit are

governed by the following equations (Saint-Venant, 1871; Chow, 1959):

$$\frac{\partial A}{\partial t} + \frac{\partial Q}{\partial x} = q \quad (2)$$

$$\frac{\partial Q}{\partial t} + \frac{\partial}{\partial x} \left(\frac{Q^2}{A} \right) + gA \frac{\partial H}{\partial x} + gAF = 0, \quad (3)$$

where t is time [T], x distance [L], g gravitational acceleration [$L T^{-2}$], F friction slope [-], H hydraulic head [L], and q [$L^2 T^{-1}$] an areal recharge or discharge flux. The friction slope F expresses the action of the wall shear stress on fluid motion and is specified in Section 2.5.3. It depends on the hydraulic radius R , which in turn is a function of the water depth y . Under free surface flow, we employ the Manning formula, and under pressurized condition the formula corresponding to the Darcy-Weisbach equation. The hydraulic head H can be decomposed into the water depth y and the bottom elevation z [L] as $H = z + y$, and the flow rate Q can be written as the product of flow velocity v times cross-sectional area A as $Q = vA$.

The cross-sectional area A is a function of the water depth y . Its functional dependence on the shape of the conduit cross-section as discussed in Section 2.5.1. With these definitions, Equations (65) and (3) can be combined into (see Appendix A)

$$\frac{\partial Q}{\partial t} = 2v \left(\frac{\partial A}{\partial t} - q \right) + v^2 \frac{\partial A}{\partial x} - gA \frac{\partial y}{\partial x} - gAF + gAB, \quad (4)$$

where $B = -dz/dx$ is the conduit bed slope [-]. The water depths at either end of the conduit are given by the nodal water depths y_{i_1} and y_{i_2} , where i_2 denotes the downstream and i_1 the upstream node.

Conduit flow can be characterized by the Froude number (Chow, 1959)

$$Fr = \frac{|v|}{\sqrt{g \frac{A}{W}}}, \quad (5)$$

which compares the impact of inertia and gravity on the flow behavior. For $Fr < 1$, gravity dominated and flow is subcritical. A perturbation of the water height propagates both in the upstream and downstream direction. For $Fr = 1$, flow is critical, a perturbation remains at the same location. For $Fr > 1$ flow is supercritical and a flow perturbation moves only downstream.

The flow system is determined by Eq. (65) and Eq. (4) where the discharge Q and the water depth y are the dependent variables and functions of distance and time. The cross-sectional area for flow A is a time-dependent and geometry-specific property depending on the water depth. Under pressurized conditions, the cross sectional area A and the flow rate Q are constant. Thus, the mass conservation statement given by Eq. (65) is trivially fulfilled, and Eq. (4) reduces to

$$-\frac{\partial y}{\partial x} + B = F, \quad (6)$$

the Darcy-Weisbach equation in the head formulation.

2.2. Space discretization

A single conduit is discretized into segments of length Δx separated by computational nodes. In order not to complicate notation, we consider the computational nodes as nodes in the network and the segments as network conduits, but keep in mind that there is a distinction between the network nodes and the computational nodes. In fact, the coordination number, that is, number of conduits connected to a node is determined by the network topology for the network nodes, and equal to 2 for the computational nodes within a conduit. In the following all nodes, computational and network nodes alike, are counted by the index i and conduits by the index l . Water depths y_i are evaluated at nodes, flow rates Q_l at conduits. Quantities that belong to a conduit l are denoted by the subscript l , for example, the discharge surface A_l and the wetted radius R_l . Conduit attributes that contribute to or are evaluated at node i are denoted by the subscripts (i, l) . For example, $Q_{i,l}$ denotes the contribution of conduit l to the flow rate at node i , and $A_{i,l}$ denotes the discharge area of conduit l evaluated using the water depth y_i at node i . Properties characterizing the geometry of the water phase at the end of the conduit, such as hydraulic radius $R_{i,l}$, width of the free water surface $W_{i,l}$, and discharge

area $A_{i,l}$ are evaluated in terms of the water depth y_i at the nodes such that,

$$A_{i,l} = A_l(y_i), \quad R_{i,l} = R_l(y_i), \quad W_{i,l} = W_l(y_i). \quad (7)$$

The functional forms of $A(y)$, $R(y)$, and $W(y)$ for circular and rectangular conduit cross-sections are given in Section 2.5.1. Conduit properties that are evaluated at the center of the conduit are determined in terms of the average water depth,

$$\bar{y}_l = \frac{y_{i_1} + y_{i_2}}{2}, \quad (8)$$

and denoted by an overbar, that is,

$$\bar{A}_l = A_l(\bar{y}_l), \quad \bar{R}_l = R_l(\bar{y}_l), \quad \bar{W}_l = W_l(\bar{y}_l). \quad (9)$$

In case of an additional upstream weighting, these quantities are marked by the subscript (α, l) . For example, the upstream weighted discharge area for conduit l is defined as

$$\bar{A}_{\alpha,l} = A_{i,l} + \alpha(\bar{A}_l - A_{i,l}), \quad (10)$$

where \bar{A}_l is the discharge area evaluated at \bar{y}_l . For $\alpha = 1$, $\bar{A}_{1,l} \equiv \bar{A}_l$. The same notation is employed for the quantities derived from the conduit properties such as the velocity $\bar{v}_l = Q_l \bar{A}_l$ and the friction slope $\bar{F}_{\alpha,l}$ which is determined from the upstream-weighted hydraulic radius $\bar{R}_{\alpha,l}$.

With these conventions, we discretize the continuity equation (65) inside the conduit as

$$\frac{dV_i}{dt} = \sum_{l=1}^2 Q_{i,l} + Q_{i,r}, \quad (11)$$

where $V_i = \Delta x A_i$ is the volume of water at node i and $Q_{i,r}$ the nodal recharge or discharge flux. Equation (11) has the same form as Eq. (1). Flow rates are defined in the conduits, water heads at the nodes. At network and computational nodes, the nodal volume V_i is a function of water head y_i [L] and thus,

$$S_i \frac{dy_i}{dt} = \sum_{l=1}^{d_i} Q_{i,l} + Q_{i,r}, \quad S_i = \frac{dV_i}{dy_i}, \quad (12)$$

where S_i denotes the nodal free surface area. It is determined as the sum of the free surface area contributions $S_{i,l}$ of the conduits l that are connected to node i ,

$$S_i = \sum_{l=1}^{d_i} S_{i,l}, \quad S_{i,l} = \frac{W_{i,l} + \bar{W}_l}{2} \frac{\Delta x}{2}. \quad (13)$$

Each conduit l connected to node i is contributing only the surface area portion up to half of its length to each node. Source terms are defined at the nodes and then interpolated to the connected conduits such that

$$Q_{i,r} = q_i d_i \frac{\Delta x}{2}, \quad \bar{q}_l = \frac{q_{i_1} + q_{i_2}}{2} = \frac{Q_{i_1,r}}{d_{i_1} \Delta x} + \frac{Q_{i_2,r}}{d_{i_2} \Delta x}. \quad (14)$$

For the spatial discretization of the momentum equation (4), we upstream weighting is applied for the pressure term and frictions slope. Furthermore, in order to improve the stability of the numerical solution, inertial damping is employed (Fread et al., 1996). This gives,

$$\frac{dQ_l}{dt} = 2\alpha \bar{v}_l \left(\frac{d\bar{A}_l}{dt} - q_l \right) + \alpha \bar{v}_l^2 \frac{A_{i_2,l} - A_{i_1,l}}{\Delta x} - g \bar{A}_{\alpha,l} \frac{y_{i_2} - y_{i_1}}{\Delta x} - g \bar{A}_{\alpha,l} \bar{F}_{\alpha,l} + g \bar{A}_l \bar{B}_l. \quad (15)$$

Recall that i_2 denotes the downstream and i_1 the upstream nodes. Both upstream weighting and inertial damping are determined by the parameter α , which depends on the local Froude number as outlined in the following. With this space discretization, flow in the network is described by Equations (12) and (15) supplemented by constitutive relations for the wetted discharge area $A_{i,l}$, free surface area $S_{i,l}$, and friction slope F_l , detailed in Section 2.5.

Upstream weighting and inertial damping

In order to improve numerical stability, upstream weighting and inertial damping (Fread et al., 1996; Rossman and Huber, 2017) are implemented in the spatially discrete momentum equation (4). The value of α , which determines both the upstream weighting of the pressure term and friction slope as well as the damping depends on the value of the local Froude number, which is defined in terms of the average flow velocity $|\bar{v}_l|$, discharge area \bar{A}_l and free surface width \bar{W}_l as

$$Fr_l = \frac{|\bar{v}_l|}{\sqrt{g \bar{A}_l / \bar{W}_l}}, \quad (16)$$

Recall that for $Fr_l < 1$ the flow is in a sub-critical state, that is, gravitational forces dominate and flow is stable. For $Fr_l > 1$ the flow is in a supercritical state dominated by inertial forces and surface waves move in the direction of the flow gradient. In this case, the average discharge area and average hydraulic radius are upstream weighted. The weight α is set to one for subcritical conditions and zero for supercritical. It interpolates linearly between one for $Fr_l = 0.5$ and zero for $Fr_l = 1$, that is,

$$\alpha = \begin{cases} 1 & \text{for } Fr_l \leq 0.5 \\ 2(1 - Fr_l) & \text{for } 0.5 < Fr_l < 1 \\ 0 & \text{for } Fr_l \geq 1 \end{cases}. \quad (17)$$

Under pressurized flow conditions α is set to zero, that is, no upstream weighting occurs and inertia terms are suppressed in line with the Darcy-Weisbach equation for pressurized conduit flow.

2.3. Time discretization

The continuity equation (12) is discretized in time using a Crank-Nicholson scheme

$$y_i^{k+1} = y_i^k + \frac{\Delta t}{S_i^{k+1}} \frac{1}{2} \left(\sum_{l=1}^{d_i} Q_{i,l}^{k+1} + Q_{i,r}^{k+1} + \sum_{l=1}^{d_i} Q_{i,l}^k + Q_{i,r}^k \right). \quad (18)$$

The indices k in the following count the time steps. The momentum conservation equation (15) is discretized using a backward Euler scheme,

$$\begin{aligned} \frac{Q_l^{k+1} - Q_l^k}{\Delta t_k} &= 2\alpha \bar{v}_l^{k+1} \left(\frac{\bar{A}_l^{k+1} - \bar{A}_l^k}{\Delta t_k} - q_l^{k+1} \right) + \alpha (\bar{v}_l^{k+1})^2 \frac{A_{i_2,l}^{k+1} - A_{i_1,l}^{k+1}}{\Delta x} \\ &\quad - g \bar{A}_{\alpha,l}^{k+1} \frac{y_{i_2}^{k+1} - y_{i_1}^{k+1}}{\Delta x} - g \bar{A}_{\alpha,l}^{k+1} \bar{F}_{\alpha,l}^{k+1} + g \bar{A}_l^{k+1} \bar{B}_l, \end{aligned} \quad (19)$$

where the time increment Δt_k may vary with the time step k as discussed below. In this discretization scheme, pressurized flow conditions are not well-defined. A node pressurizes if the discharge area A_l becomes equal to the conduit area, and the respective free surface area goes to zero. Thus, under pressurized conditions, the water depth y_i cannot be updated by Eq. (18). In order to circumvent this difficulty, small but finite free surface areas $S_{i,l}$ are assigned to pressurized conduits using the concept of the Preissmann slot (Cunge and Wegner, 1966). Details are given in Section 2.5.2.

Time step

The time step size is computed according to an adaptive scheme based on the value of the local Froude number Fr_l (Rossman and Huber, 2017). To this end, we define the time increment

$$\Delta t_l \leq Cr \left(\frac{Fr_l}{1 + Fr_l} \right) \frac{D_l}{|\bar{v}_l|}, \quad (20)$$

where D_l is the hydraulic diameter of conduit l and Cr the Courant number, which is set here equal to 1 for free surface and to 1/2 for pressurized flow. Highly dynamic flows often require stricter constraints, typically setting (free surface flow) $Cr < 1$ and (pressurized flow) $Cr < 1/2$ to ensure numerical stability. For steadier and less erratic flow dynamics, it may be feasible to relax the constraints and set $Cr \geq 1$ without losing accuracy in the simulation. Furthermore, we define time increment Δt_i based on the rate of change in water depth relative to the maximum conduit diameter $D_i^m = \max_l(D_{i,l})$ connected to the node

$$\Delta t_i \leq \Delta t_k \frac{D_i^m}{y_i^{k+1} - y_i^k}, \quad (21)$$

where Δt_k is the current time step. The time increment Δt_{k+1} at the time step $k+1$ is then determined as the minimum value of all Δt_l and Δt_i ,

$$\Delta t_{k+1} = \min_{l,i}(\Delta t_l, \Delta t_i). \quad (22)$$

2.4. Picard iteration

Equations (18) and (19) form a coupled non-linear system, which can be written as

$$\mathbf{y}^{k+1} = \mathbf{F}(\mathbf{y}^k, \mathbf{y}^{k+1}, \mathbf{Q}^k, \mathbf{Q}^{k+1}) \quad (23)$$

$$\mathbf{Q}^{k+1} = \mathbf{G}(\mathbf{y}^k, \mathbf{y}^{k+1}, \mathbf{Q}^k, \mathbf{Q}^{k+1}). \quad (24)$$

We defined the vectors $\mathbf{y} = (y_1, \dots, y_{N_o})^\top$ and $\mathbf{Q} = (Q_1, \dots, Q_{N_c})^\top$, where the subscript \top denotes the transpose. The system is solved using the relaxed Picard iteration (Langtangen and Linge, 2017)

$$\hat{\mathbf{Q}}^{j+1} = \mathbf{G}(\mathbf{y}^k, \mathbf{y}^{k,j}, \mathbf{Q}^k, \mathbf{Q}^{k,j}) \quad (25)$$

$$\mathbf{Q}^{k,j+1} = \omega \hat{\mathbf{Q}}^{j+1} + (1 - \omega) \mathbf{Q}^{k,j} \quad (26)$$

$$\hat{\mathbf{y}}^{k,j+1} = \mathbf{F}(\mathbf{y}^k, \mathbf{y}^{k,j}, \mathbf{Q}^k, \mathbf{Q}^{k,j+1}) \quad (27)$$

$$\mathbf{y}^{k,j+1} = \omega \hat{\mathbf{y}}^{j+1} + (1 - \omega) \mathbf{y}^{k,j} \quad (28)$$

for the initial values $\mathbf{y}^{k,j=0} = \mathbf{y}^k$ and $\mathbf{Q}^{k,j=0} = \mathbf{Q}^k$. The index j counts the Picard iterations. The relaxation factor ω assumes values between 0 and 1. The value of ω is set to 0.8 by default but can be lowered to ensure convergence and limit the occurrence of oscillations. The iteration stops when the convergence criterion in terms of subsequent water heads is reached. That is, convergence is reached when the absolute differences between all the elements of the current water depths vector, $\mathbf{y}^{k,j+1}$, and the corresponding elements of the previous water depths vector, $\mathbf{y}^{k,j}$, are smaller than a tolerance δ ,

$$\text{Convergence} \quad \text{if} \quad \forall i, \quad \left| y_i^{k+1,j+1} - y_i^{k+1,j} \right| < \delta. \quad (29)$$

The maximum number of Picard iterations is set to 20 by default, and the tolerance to $\delta = 10^{-8}$. If convergence is reached, $\mathbf{Q}^{k+1} = \mathbf{Q}^{k,j+1}$ and $\mathbf{y}^{k+1} = \mathbf{y}^{k,j+1}$. The Picard iteration for the next time step starts.

Drying and rewetting dynamics of conduits

Analogous to the challenges of modeling pressurized conduits, the drying and rewetting dynamics also require numerical approximations to effectively address limitations of the governing equations when water depths become zero or negative. When this occurs, Eq. (19) cannot be solved because then the hydraulic radius $R = 0$ and thus the

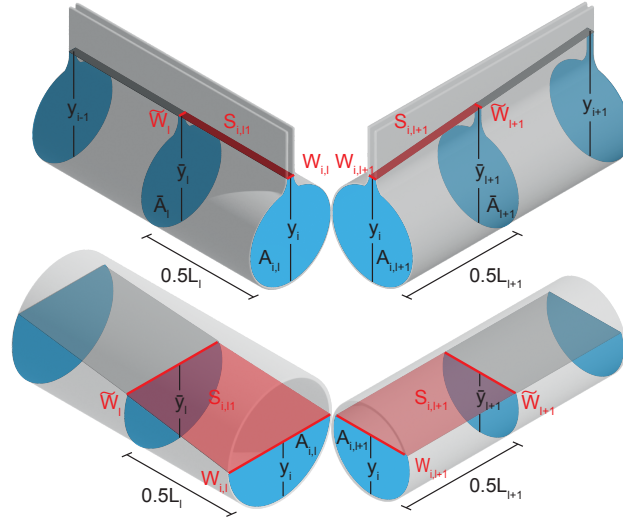


Figure 2: Computation of hydraulic parameters for a pressurized system including a Preissman slot (top) and free-surface system (bottom) of two conduits connected at node y_i . The Preissmann slot is not to scale. Note that other combinations of pressurized and free surface conditions may exist and more than one conduit may be connected to a node. Switching to pressurized flow computation using the Darcy-Weisbach equation is based on the pressurization state at \bar{y} only.

friction slope F is not defined. Therefore we set a global lower limit for the water depth of $y_{min} = 1 \times 10^{-12}$ m, which sustains a finite but negligible flow component within conduits. Nodes with $y_i^{k,j+1} < y_{min}$ are considered dry. To avoid outflow from dry nodes we check after each Picard iteration if the nodes at either end of a conduit satisfy $y_i^{k,j+1} \leq y_{min}$. If this is the case, the flow rate of that conduit is set to $Q_i^{k,j+1} = Q_{min} = 1 \times 10^{-12} \text{ m}^3 \text{ s}^{-1}$ keeping the flow direction, and the water depth is set $y_i^{k,j+1} = y_{min}$, which prevents negative water depths.

2.5. Closure Relations

Here we define the closure relations to determine the discharge area A , width W of the free water surface and the wetted perimeter P of the conduit from the water depth and the conduit geometry. We assume here that the conduits have a circular cross section with constant diameter D . Furthermore, we define the Preissmann slot for the modeling of pressurized flow and give the formulae for the friction slope F .

2.5.1. Computation of free surface and discharge areas

The computation of nodal free surface areas to update water depths via Eq. (18), conduit discharge areas and hydraulic radii required in Eq. (19) represents one of the most computationally demanding tasks within the code. The hydraulic parameters depend on the specific geometry of the conduits. For any cross-sectional shape the surface area A , surface width W and the perimeter P are a function of the water depth y (see Fig. 2). The functional relations may strongly vary for circular, rectangular or trapezoidal geometries. For more complex geometries there may not be closed form analytical expressions. In these case, A , W and R are determined numerically and their dependence on y is tabulated.

In the current code version we implement circular and rectangular conduits with constant diameter D or width b and length L . For the rectangular conduits, the width of the free surface, discharge area, wetted perimeter and hydraulic radius are given by

$$W(y) = b, \quad A(y) = by, \quad P(y) = b + 2y, \quad R(y) = \frac{by}{b + 2y}. \quad (30)$$

For circular conduits, the free surface width W is expressed in terms of the water depth y as

$$W(y) = \begin{cases} W_0 & \text{if } y \geq D \\ 2\sqrt{Dy - y^2} & \text{if } y < D \end{cases}, \quad (31)$$

where W_0 is the virtual surface width, or Preissman slot (Preissmann, 1961), required to deal with pressurized flow conditions as discussed in the next section. The discharge area A is determined in terms of the water depth as

$$A(y) = \begin{cases} \pi R^2 + (y - D)W_0 & \text{if } y \geq D \\ R^2 \frac{\theta(y) - \sin \theta(y)}{2} & \text{if } y < D \end{cases}, \quad (32)$$

where R [L] is the radius of the conduit and

$$\theta(y) = \begin{cases} 2\pi & \text{if } y \geq D \\ 2 \arccos \left(\frac{R-y}{R} \right) & \text{if } y < D \end{cases}. \quad (33)$$

The wetted perimeter P and hydraulic radius are

$$P(y) = R\theta(y), \quad R(y) = \frac{A(y)}{P(y)}. \quad (34)$$

2.5.2. Preissmann slot

When nodes or conduit centers become pressurized, that is, if the water depth y_i at a node exceeds the maximum diameter of all the connected conduits, or when \bar{y}_l at a conduit center exceed the conduit diameter, the computation of the free surface areas S and thus also the discharge area A must be modified. A conduit is considered pressurized if $\bar{y}_l \geq D_l$, a node is considered pressurized if the nodal water depth is larger than or equal to the maximum diameter of the conduits that are connected to it, $y_i \geq \max_l(D_{i,l})$. As the pressurization state of a conduit is determined based on the average water depth \bar{y}_l , it can happen that the conduit is pressurized at one end (if $y_i > D_{i,l}$), while it is considered in free surface flow mode because $\bar{y}_l < D_l$. The flow mode of the conduit is important for the switching between two different friction slopes, as detailed in the next section.

If a node and the connected conduits pressurize, the nodal free surface area S_i defined by Eq. (13) becomes zero. Thus, it is not possible to update the nodal water depth y_i using Eq. (18). In order to circumvent this problem, a virtual water depth and hence an extended free surface area is computed by assigning a finite value to the free surface width $W = W_0$ when $y \geq D$, which is the width of the so-called Preissmann slot (Cunge and Wegner, 1966). Adding this virtual storage is equivalent to considering the water as slightly compressible.

For $y > D$ but below a critical threshold, the virtual slot widths W_0 is determined following Sjöberg (1982) and Rossman and Huber (2017). When y exceeds a critical value of $y_c = 1.78D$, the slot width is set equal to 1% of the conduit diameter D (see Fig. 3, left). That is,

$$W_0(y, R) = \begin{cases} 0.5423 \exp(-(y/D)^{2.4}) D & \text{for } D \leq y \leq y_c \\ 0.01D & \text{for } y > y_c \end{cases}. \quad (35)$$

If both node and connected conduits are pressurized, the nodal free surface area S_i is non-zero because it is computed in terms of the virtual slot widths $W_0(y_i, R_l)$ and $W_0(\bar{y}_{i,l}, R_{i,l})$. The respective discharge areas for pressurized flow are extended by the additional area due to the slot above the conduit ceiling as given in Eq. (32), see also Fig. 3. The hydraulic perimeter and hydraulic radius are not recalculated for the Preissmann slot because its impact is negligible.

2.5.3. Friction slope

The friction slope can be quantified by the Manning or Darcy-Weisbach equations. The Manning formula for the friction slope reads as

$$F = \frac{h_f}{L} = n^2 \frac{Q|v|}{AR^{4/3}}, \quad (36)$$

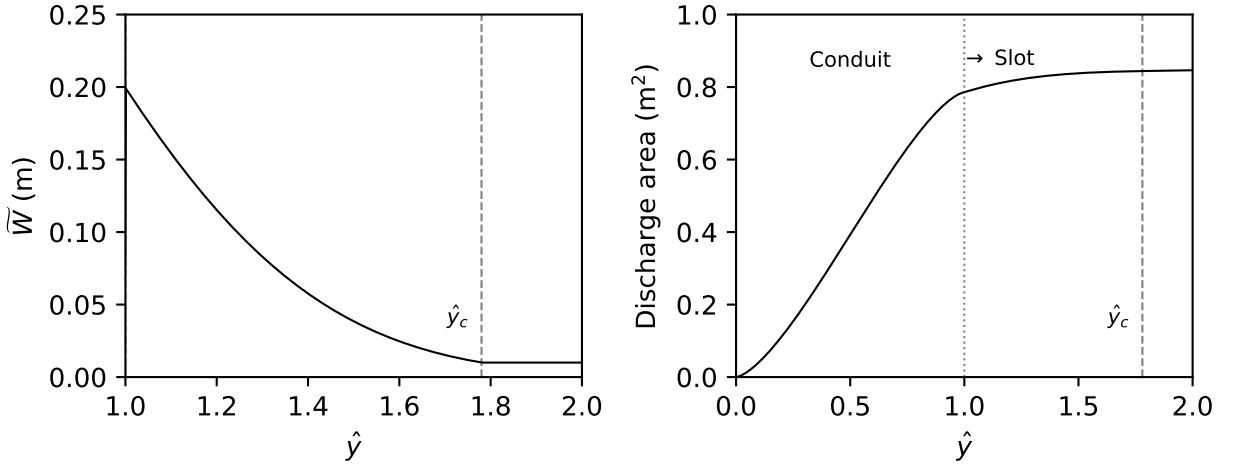


Figure 3: (Left) Evolution of the slot width under pressurized conditions for a conduit with diameter $D = 1$ m. A constant slot width of $W_0 = 0.01D$ is reached at $y_c = 1.78D$. (Right) Evolution of the discharge area in a conduit with $D = 1$ m. Beyond a normalized depth of $y = D$, the additional contribution is due to the Preissmann slot.

where $h_f [L]$ is the head loss along distance $L [L]$, n is the Manning friction coefficient [$TL^{-1/3}$] and R is the hydraulic radius [L]. The Darcy-Weisbach equation results in the following friction slope,

$$F = \frac{f_D v^2}{8gR}. \quad (37)$$

where f_D is the dimensionless friction coefficient. Under laminar conditions ($Re < 2300$) the friction factor is

$$f_D = \frac{64}{Re}, \quad (38)$$

where the Reynolds number is defined as

$$Re = \frac{\rho |\bar{v}| D}{\mu} \quad (39)$$

with $\rho = 1000 \text{ m}^3 \text{ s}^{-1}$ the water density and $\mu = 0.001 \text{ kg m}^{-1} \text{ s}^{-1}$ the dynamic viscosity. For turbulent conditions various models such as the Colebrook-White equation (Colebrook and White, 1937) or Swamee-Jain formulation (Swamee and Jain, 1976) have been proposed to solve for the friction factor, i.e., when $Re > 2300$. As these formulations implicitly depend on f they are often solved iteratively. Here we employ an alternative formulation after Churchill (1977), which allows a continuous explicit calculation of the friction factor under both laminar and turbulent conditions (see Fig. 4):

$$f_D = 8 \left[\left(\frac{8}{Re} \right)^{12} + \frac{1}{\Omega_1 + \Omega_2} \right]^{\frac{1}{12}} \quad (40)$$

$$\Omega_1 = \left[-2.457 \ln \left(\left(\frac{7}{Re} \right)^{0.9} + 0.27 \frac{\epsilon}{d} \right) \right]^{16} \quad (41)$$

$$\Omega_2 = \left(\frac{37530}{Re} \right)^{16}, \quad (42)$$

where $\epsilon [L]$ is the effective conduit roughness height and ϵ/D is referred to as the relative roughness $[-]$.

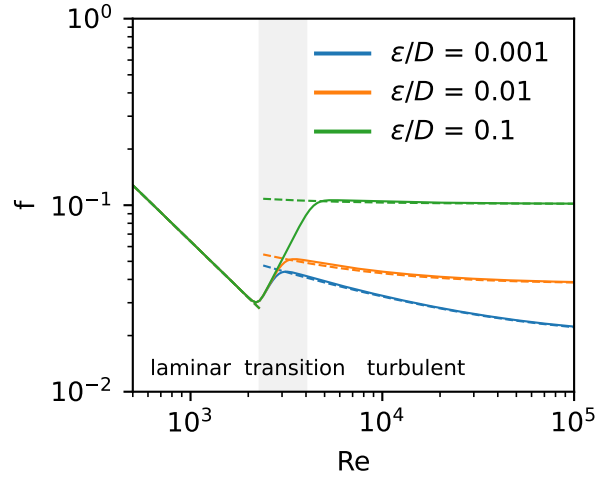


Figure 4: Friction factor f for a range of Reynolds numbers and three values of the relative roughness ϵ/D . Solid lines represent the continuous Churchill equation, while dashed lines the Colebrook-White equation. The shaded area marks the transition region between laminar and turbulent conditions ($2300 \geq Re \geq 4000$).

Under free surface flow conditions, the friction slope in Eq. (19) is set equal to the Manning formula (36) and under pressurized conditions, it is set equal to the Darcy-Weisbach formula (37). In order to allow for a continuous computation during transitions from free surface to pressurized conditions with a single descriptor for the roughness properties we define a Manning coefficient that is consistent with the Darcy-Weisbach friction factor. Thus, we equate equations (37) and (36) for the same velocity v in order to derive

$$n = \sqrt{\frac{f_D R^{\frac{1}{3}}}{8g}}. \quad (43)$$

Note that this equation implies that the Manning coefficient depends on Re through the dependence of the Darcy friction factor f_D on Re . Thus, we define a unique Manning coefficient by setting $f_D = f_D(Re = \infty)$ in Eq. (43).

2.6. Boundary and initial conditions

Head boundary conditions at inflow or outflow nodes are enforced by setting the water depth $y_i^{k,j+1}$ equal to the corresponding fixed water depth $y_{i,f}$ after each Picard iteration

$$y_i^{k,j+1} = y_{i,f}. \quad (44)$$

Flux boundary conditions at inflow or outflow nodes are imposed on the total nodal flux, which is defined by

$$Q_i = \sum_{l=1}^{d_i} Q_{i,l}. \quad (45)$$

Using this notation, the continuity equation (18) reads as

$$y_i^{k+1} = y_i^k + \frac{\Delta t}{S_i^{k+1}} \frac{1}{2} (Q_i^{k+1} + Q_i^k). \quad (46)$$

A prescribed flux value $Q_{i,f}$ at a boundary node i is enforced by setting $Q_i^{k,j+1}$ at each Picard iteration equal to

$$Q_i^{k,j+1} = \sum_{l=1}^{d_i} Q_{i,l}^{k,j+1} + Q_{i,f}. \quad (47)$$

This implies that under steady-state conditions the sum of the fluxes in the conduits connected to node i is $Q_i = -Q_{i,f}$.

Initial conditions must be set for the water depth y_i at the nodes and the flow rate Q_l in the conduits. By default, all values are initially set to zero.

3. Verification and validation

In the following subsections we first verify the developed model through a series of analytical tests. We consider steady-state conditions, different geometries and boundary conditions, as well as free surface and pressurized flows. For the first three cases we conduct a convergence study with respect to the resolution Δx using the percentage root mean square error (RMSE) as an accuracy metric. Finally we compare the code to a laboratory experiment in order to validate the correct implementation of the full dynamic wave equation under transient conditions. Equilibrium conditions for the steady-state cases at $t = 5000$ s are computed with a time step size $dt = 0.1$ s. All cases used an under-relaxation of $w = 0.8$. Initial conditions are $y = 0$ m and $Q = 0$ m³s⁻¹ unless otherwise specified. The water density is set to $\rho = 1000$ m³s⁻¹ and the dynamic viscosity is $\mu = 0.001$ kgm⁻¹s⁻¹.

3.1. Steady-state free surface channel flow

In this section, we verify the numerical implementation for free surface flow in a rectangular channel under steady state conditions. The governing equations (65) and (4) then reduce to

$$\frac{\partial Q}{\partial x} = q \quad (48)$$

$$\frac{Q^2}{gA^3} \frac{\partial A}{\partial x} - \frac{\partial y}{\partial x} - \frac{2Qq}{A} - F + B = 0, \quad (49)$$

where we used that $Q = vA$. Equation (49) provides an equation for the bedslope B in terms of a given water depth, which can be written as

$$\frac{dz}{dx} = \left(\frac{Q^2}{gA^3} \frac{dA}{dy} - 1 \right) \frac{\partial y}{\partial x} - \frac{2Qq}{gA^2} - F. \quad (50)$$

Note that $Q = Q_f + qx$, where Q_f is the prescribed flow rate at the left boundary. The rectangular channel has width b such that the discharge area and the hydraulic radius are

$$A(y) = by, \quad R(y) = \frac{by}{b + 2y}. \quad (51)$$

We define the flow rate and recharge rate per channel width as $Q' = Q/b$ and $r_0 = q/b$. Thus, we can write Eq. (50) as

$$\frac{dz}{dx} = \left(\frac{Q'^2}{gy^3} - 1 \right) \frac{\partial y}{\partial x} - \frac{2Q'r_0}{gy^2} - F, \quad Q' = Q'_f + r_0x. \quad (52)$$

For a broad channel with $b \gg y$, we can set $R = y$ and the Manning friction slope given by Eq. (36) becomes

$$F(y) = \frac{n^2 Q' |Q'|}{y^{\frac{10}{3}}}. \quad (53)$$

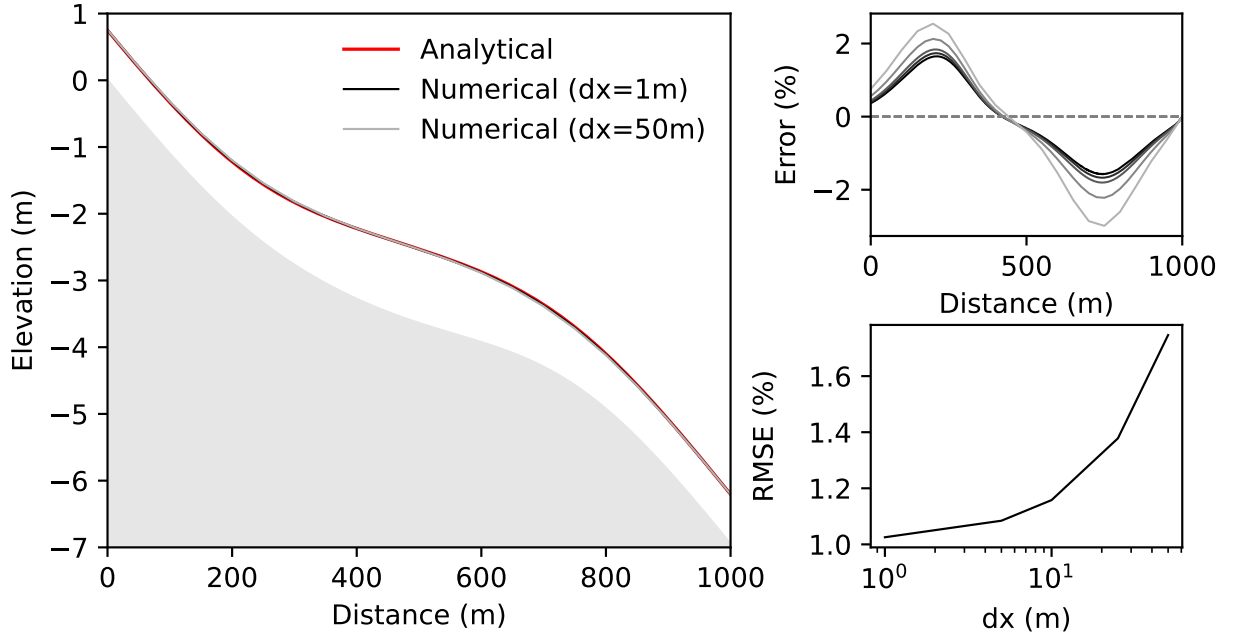


Figure 5: Comparison of the numerical solution for the water depth at steady-state with the analytical solution Eq. (58) for different resolutions $\Delta x = 1, 5, 10, 25$ and 50 m. Notice that the channel base (lightgray) is only shown for a resolution of $\Delta x = 1$ m. Errors are shown for all resolutions with lighter gray for higher values of Δx . RMSE values are computed based on the percentage errors.

Following Delestre et al. (2013), we prescribe the water depth $y_0(x)$, from which we can obtain the bottom slope $z(x)$ by integration of Eq. (50) from 0 to x as

$$z(x) = \int_0^x dx' \left\{ \left(\frac{Q'^2}{gy_0(x')^3} - 1 \right) \frac{\partial y_0(x')}{\partial x'} - \frac{2Q'r_0}{gy_0(x')^2} - F[y_0(x')] \right\}. \quad (54)$$

In the following, we numerically solve the Saint-Venant equations

$$\frac{\partial y}{\partial t} + \frac{\partial Q'}{\partial x} = 0 \quad (55)$$

$$\frac{\partial Q'}{\partial t} = 2v \left(\frac{\partial y}{\partial t} - r_0 \right) + v^2 \frac{\partial y}{\partial x} - gy \frac{\partial y}{\partial x} - gyF + gyB \quad (56)$$

with the bedslope

$$B = - \left(\frac{Q'^2}{gy_0(x)^3} - 1 \right) \frac{\partial y_0(x)}{\partial x} + \frac{2Q'r_0}{gy_0(x)^2} + F[y_0(x)] \quad (57)$$

for a given $y_0(x)$ as specified below. The numerical steady state solution is then compared to the exact $y_0(x)$.

3.1.1. Gaussian profile

In this verification example, we consider free surface flow without recharge, that is, $r' = 0$, in a channel of length $L = 1000$ m with the prescribed equilibrium profile given by the Gaussian-shaped function (Delestre et al., 2013)

$$y_0(x) = \left(\frac{4}{g}\right)^{\frac{1}{3}} \left(1 + \frac{1}{2} \exp \left[-16 \left(\frac{x}{1000} - \frac{1}{2} \right)^2 \right] \right). \quad (58)$$

At the left boundary at $x = 0$ m we specify the flow rate $Q'_f = 2.0 \text{ m}^2\text{s}^{-1}$. At the right boundary we set the constant water depth $y_f = y_0(1000 \text{ m}) = 0.7483$ m. We consider channel discretizations of length $\Delta x = 1, 5, 10, 25$ and 50 m. The Manning roughness coefficient is set to $n = 0.033 \text{ m}^{-1/3}\text{s}$. The initial height distribution is set to $y(x, t = 0) = 0$ m. The numerical simulations converge to steady state after the time $t = 5000$ s.

The comparison of the numerical and the analytical solution is shown in Fig.(5). Its demonstrates good agreement and a maximum error of about $\pm 1.8 \%$ for the highest resolution of $\Delta x = 1$ m near the steepest parts of the channel. For the lowest resolution with $\Delta x = 50$ m the results are still acceptable with an error of about $\pm 2.5 \%$. The percentage RMSE converges towards an error of $\pm 1 \%$ at the highest resolution and increases to about $\pm 1.7 \%$ for the lowest resolution.

3.1.2. Wavy profile

Next we consider a verification example of free surface flow in a channel of length $L = 5000$ m for $r_0 = 0$ for the sinusoidal steady state profile

$$y_0(x) = \frac{9}{8} + \frac{1}{4} \sin \left(\frac{10\pi x}{L} \right) \quad (59)$$

At the left boundary at $x = 0$ m, we set the constant inflow $Q_f = 2.0 \text{ m}^2\text{s}^{-1}$. At the right boundary at $x = 5000$ m we specify the constant depth $y_f = y_0(1000 \text{ m}) = 1.125$ m. The channel is discretized into segments of length $\Delta x = 1, 5, 10, 50, 100$ and 200 m. The Manning roughness coefficient is set to $n = 0.03 \text{ m}^{-1/3}\text{s}$. The initial height distribution is set to $y(x, t = 0) = 0$ m. The numerical simulations converge to steady state after the time $t = 4000$ s. The analytical and numerical solutions are compared in Fig. 6. We obtain good agreement with a maximum error of about $\pm 1.8 \%$ close to regions of highest slope along the sinusoidal channel (see). For the lowest resolution of $\Delta x = 200$ m absolute errors are slightly higher at about 6% . The percentage RMSE drops to less than 0.7% at the highest resolution and remains under 3% for the lowest resolution at $\Delta x = 200$ m.

3.1.3. Steady free surface flow with diffuse recharge

To verify the implementation of the diffuse recharge we simulate flow in a channel of length $L = 1000$ m with a specified constant inflow boundary condition at the left boundary $x = 0$ m with $Q_f = 1.0 \text{ m}^2\text{s}^{-1}$ and a constant water depth at the right boundary with $y = y_{eq}(1000 \text{ m}) = 0.7483$ m. The channel segments are of length $\Delta x = 1$ m. The Manning roughness coefficient is set to $n = 0.033 \text{ m}^{-1/3}\text{s}$. Diffuse recharge is applied to all nodes $0 \leq x \leq L$ with $r_0 = 0.001 \text{ ms}^{-1}$. The steady state water depth $y_0(x)$ is given by the Gaussian-shaped function (58). The numerical model correctly recovers the depth profile along the channel with absolute errors less than about $\pm 4 \%$ (see Fig. 7) at the highest resolution. Similar to the previous examples the highest deviation can be observed close to the steepest slopes of the system, except towards the right boundary where errors are converging towards zero due to the applied constant head boundary. For the lowest resolution of $\Delta x = 50$ m absolute errors are still below 6% . Percentage RMSE errors drop below 3.5% with increasing resolution and are at about 4.6% at the lowest resolution of $\Delta x = 50$ m.

3.2. Steady-state flow in circular conduit under pressurized conditions

Here we consider steady-state flow through a horizontal conduit system comprising ten conduit segments each with a length $\Delta x = 100$ m, resulting in a total length of $L = 1000$ m. The conduits have a constant diameter of $D = 1$ m and a base elevation of $z = 0$ m. At the right boundary ($x = 1000$ m) we maintain a constant water level $y = 1.1$ m. At the left boundary ($x = 0$ m) we specify water depths in a range from $y = 1.15$ m to $y = 5$ m to establish varying pressure gradients for each equilibrium condition. Initial conditions are $y = 0.9$ m at the left boundary and $y = 0.8$ m at the right boundary, i.e., flow is initially non-pressurized. The initial discharge is $Q = 0 \text{ m}^2\text{s}^{-1}$ and three values for

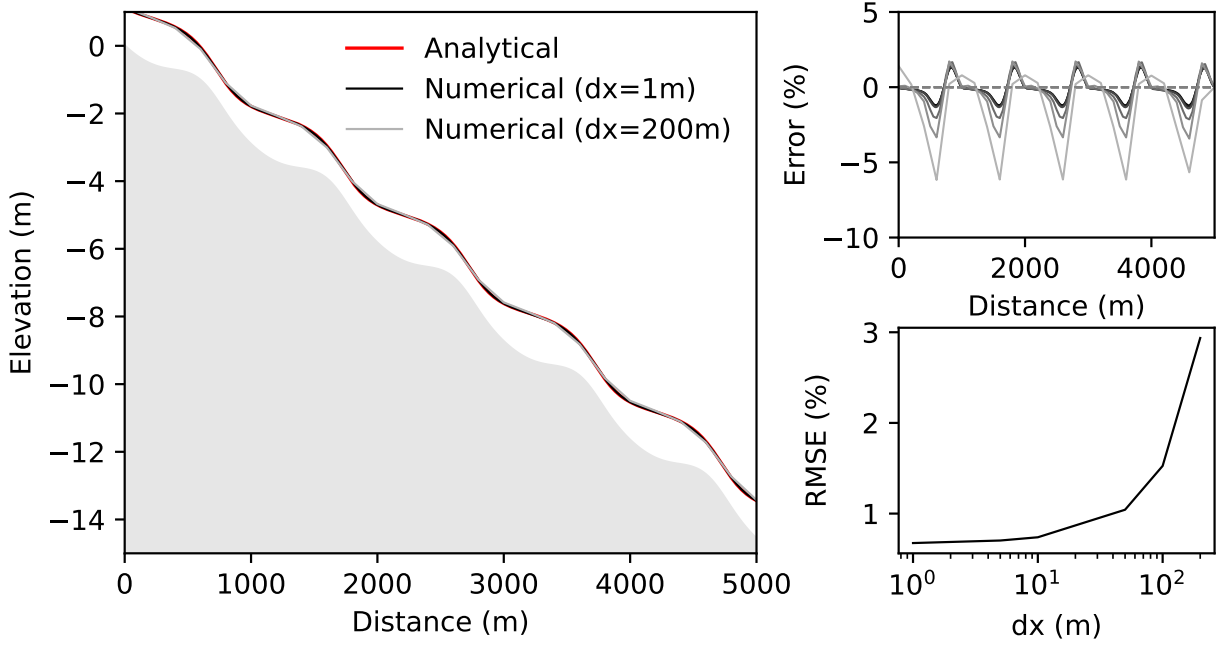


Figure 6: Comparison of the numerical solution for the water depth at steady-state with the analytical solution Eq. (59) for different resolutions $\Delta x = 1, 5, 10, 50, 100$ and 200 m. Notice that the channel base (lightgray) is only shown for a resolution of $\Delta x = 1$ m. Errors are shown for all resolutions with lighter gray for higher values of Δx . RMSE values are computed based on the percentage errors.

the Darcy-Weisbach roughness height are chosen as $\epsilon = 0.001, 0.01$ and 0.1 m. Equilibrium conditions are computed at $t = 4000$ s.

The numerical results are compared to the Darcy-Weisbach equation

$$\frac{\Delta P}{L} = f_D \frac{\rho}{2D} \left(\frac{Q}{A_p} \right)^2 \quad (60)$$

where A_p is the pressurized discharge area extended by the additional contribution from the virtual slot (see Eq. 33 and 32),

$$A_p = \pi \frac{D^2}{4} + \frac{1}{N_c} \sum_{l=1}^N (\bar{y}_l - D_l) W_0(\bar{y}_l), \quad (61)$$

where $N_c = 100$ is the total number of segments l .

Given a pressure differential ΔP along the distance L based on specified constant water depths at the left and right boundaries and the surface roughness ϵ we iteratively solve Eq. (60) to compute the corresponding discharge Q . Figure 3.2 shows the numerical solution and the analytical solution for three roughness values. Good agreement is found over the whole range of considered pressure drops and Reynolds numbers. Errors exhibit a slight increase as Reynolds numbers rise but remain below 2 %. The stronger variation in errors for lower pressure drops and Reynolds numbers can be explained by the chosen water depths at the left boundary, which here result in most nodes of the conduit being below or close to the critical height \hat{y}_c so that the slot width determined according to Eq. (35).

3.3. Transient free surface flow with diffuse recharge

Analytical solutions for the full dynamic wave model, which retains all terms of the momentum equation Eq. (3), are extremely challenging to derive, even for simple geometries and boundary conditions. Therefore various simplifications

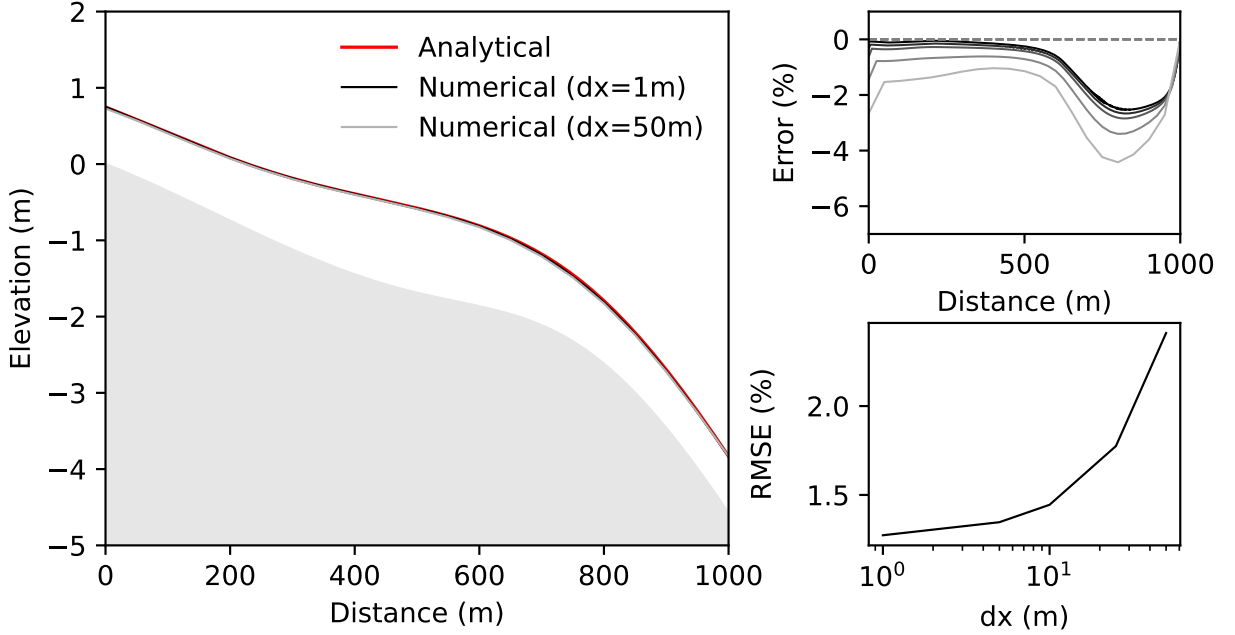


Figure 7: Comparison of the numerical solution for different resolutions $\Delta x = 1, 5, 10, 25$ and 50 m for the water depth at steady-state with the analytical solution Eq. (58). A steady diffuse recharge of $r_0 = 0.001 \text{ ms}^{-1}$ is applied along the whole domain. Notice that the channel base (lightgray) is only shown for a resolution of $\Delta x = 1$ m. Errors are shown for all resolutions with lighter gray for higher values of Δx . RMSE values are computed based on the percentage errors.

have been proposed. For many flood routing applications in natural channels, the acceleration terms of the Saint-Venant equation are often omitted, leading to the diffusive wave model (Hayami, 1951). This single parabolic equation captures only diffusive transport processes of the flow dynamics. Wave velocity and diffusivity in this model are treated as constants. A further simplification can be obtained by removing the water depth gradient, which yields the so called kinematic wave equation.

In order to validate the transient flow dynamics under consideration of all terms of the momentum equation Eq. (4) and allow for spatial and temporal variation of wave velocity and diffusivity, we compare our code to the laboratory experiment of Delestre et al. (2013). The experiment consists of an inclined metal channel with a total length of $L = 4$ m and a width of $b = 0.12$ m. The slope of the channel is $B = 4.96\%$ and a constant rainfall of $P = 50.76 \text{ mmh}^{-1}$ is applied along the channel reach for times $t \in [5, 125 \text{ s}]$ and within distance $x \in [0, 3.95 \text{ m}]$. In the numerical simulations the computation of the discharge areas ($A = by$) and hydraulic radius are adapted to a rectangular channel structure, that is,

$$R = \frac{by}{b + 2y} \quad (62)$$

The channel is discretized with 100 segments of length $\Delta x = 0.04$ m. The base of the channel is dropping linearly from a height of $z = 0.1984$ m at $x = 0.0$ m to a height of $z = 0.0$ m at $x = 4.0$ m. Initial conditions are $y = 0$ m and $Q = 0 \text{ m}^2\text{s}^{-1}$ at all nodes. To simulate a outfall condition a constant water depth $y = 0.0$ m is prescribed at the right boundary ($x = 4.0$ m). Simulations are run with a time step size $dt = 0.05$ s to a maximum time of $dt = 250$ s. A constant precipitation $P_c = 1.44 \times 10^{-5} \text{ ms}^{-1}$ is applied at times $5 \text{ s} < t < 125 \text{ s}$, resulting in a volumetric flux of $Q_r = 1.44 \times 10^{-5} \text{ ms}^{-1} \times (0.12 \text{ m} \times 0.04 \text{ m}) = 6.933 \times 10^{-8} \text{ m}^3\text{s}^{-1}$ at all channel segments. Note that, in line with Delestre (2010) a corrected precipitation of $P = 52 \text{ mmh}^{-1}$ is assumed in the simulations.

Similar to Delestre (2010) we find that a Manning roughness coefficient of $n = 0.013 \text{ m}^{-1/3}\text{s}$ reproduces the experimental data with satisfactory accuracy (see Fig. 9). The initial peaks in discharge at about $dt = 40$ s and fluctuations along the period of constant discharge are most likely a result of preferential flow formation, i.e. instabilities

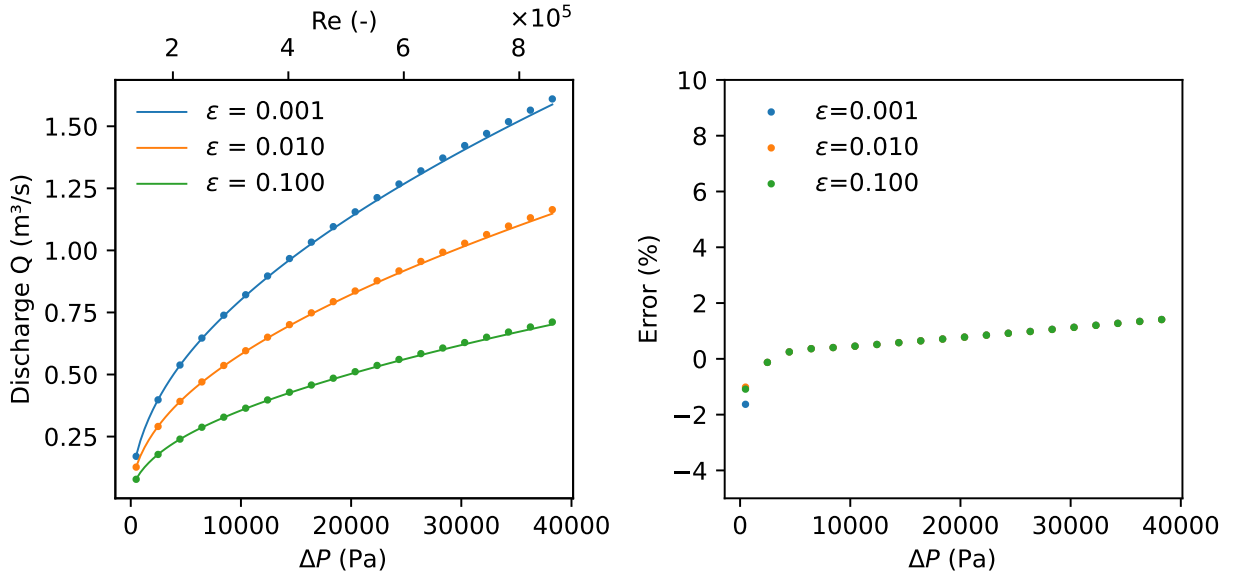


Figure 8: Comparison of steady-state discharge for three different roughness coefficients under pressurized flow conditions in a conduit of length $L = 1000$ m with $\Delta x = 100$ m (left) and corresponding errors (right). Circles represent the numerical solution obtained at an equilibrium at $t = 2000$ s and lines the analytical solution computed with Eq. (60).

along the channel width. Due to the chosen 1D modeling approach they can not be recovered in the simulations, which was also noted by Ersoy et al. (2020). The cumulative discharge mass also shows good agreement with the experimental data and closely aligns with the results obtained by Delestre (2010) and Ersoy et al. (2020).

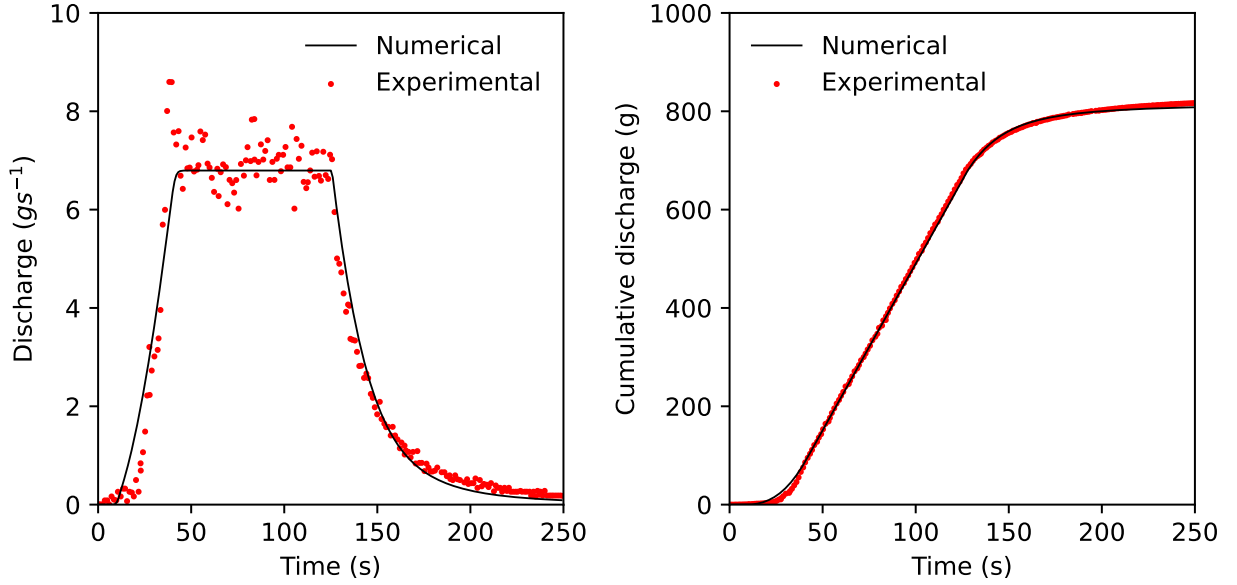


Figure 9: Comparison of the numerical solution for the discharge and cumulative discharge with the experimental data of Delestre (2010) under consideration of a constant diffuse recharge of $R_c = 52 \text{ mmh}^{-1}$ for $5 \text{ s} < t < 125 \text{ s}$ along the channel between $x = 0 \text{ m}$ and $x = 3.95 \text{ m}$. The channel is $L = 4 \text{ m}$ long with a slope of $B = 4.96 \%$, $\Delta x = 1 \text{ m}$ and $dt = 0.05 \text{ s}$. A constant water depth of $y = 0.0 \text{ m}$ is prescribed at the right boundary $x = 4.0 \text{ m}$. The Manning coefficient is set to $n = 0.013 \text{ m}^{-1/3} \text{ s}$ and initial conditions are $y = 0 \text{ m}$ and $Q = 0 \text{ m}^2 \text{ s}^{-1}$.

4. Demonstration example: Ox Bel Ha cave system, Quintana Roo, Mexico

Here we demonstrate the simulation of flow in the worldwide largest submerged cave network, the Ox Bel Ha system in Quintana Roo, Mexico. As of 2023 the official total length of the explored part of the system is 435.8 km. The average depth of the system is about 16 m with a maximum of 57.3 m. The cave system is connected to the surface via 152 cenotes (sinkholes) and has several discharge outlets towards the Carribean coast (Devos et al., 2023).

The network consists of 10098 conduits with a maximum length of 111.52 m and a minimum length of 0.6 m. For the sake of simplicity and due to absence of detailed data we assume an average diameter of all conduits of 1 m and a uniform roughness height of $\epsilon = 0.03 \text{ m}$. Injection nodes, i.e. positions where cenotes/sinkholes are present, are distributed at equal intervals based on nodal indices. Nodes close to the Carribean coast are set as constant pressure outlets. Their water depths are adjusted to a constant value in order to maintain a constant hydraulic head of $H = 2 \text{ m}$, which reflects the constant elevation of the ocean during the injection scenario.

The network system is brought to a steady-state with a constant recharge of $0.02 \text{ m}^3/\text{s}$ equally distributed over all conduits. This approximately corresponds to an average annual recharge of 180 mm/a given a catchment area of about 36 km. We then simulate a heavy storm event with an intensity of 40 mm/h. We model the input signal at each sinkhole over a time period of 2 h as a linear ramp to $0.05 \text{ m}^3/\text{s}$ at 1 h before decreasing again until 2 h (see Fig. 11, upper left). For an average sinkhole diameter of 75 m this corresponds to an injection rate of about $0.05 \text{ m}^3/\text{s}$. Due to the shallow depth of the conduit system and the rapid transfer of recharge through the sinkholes we assume an instantaneous injection at the conduit level.

Figure 10 shows the Ox Bel Ha cave system shortly after the onset of the recharge event at $t = 100 \text{ s}$ (left figure) and at time $t = 6100 \text{ s}$ when the peak discharge at the spring outlets is registered (right figure). Flow rate distributions indicate two main pathways connected to outlets 1 and 3-7 close to steady-state conditions, while outlet 2 and 8-10 are activated more efficiently during peak flow conditions. At outlet 8-10 this is most likely caused by the marginal position of the branch and connectivity to the main branches in southwestern direction, which is oriented against the main flow gradient towards the southwest. Outlet 2 on the other hand is seemingly well connected to the upstream network in northwestern direction, similar to outlets 3-7. However, the majority of conduits, up to the position where the branch merges with the main branch connected to outlet 3-7, are about 10 m deeper. Therefore the branch system

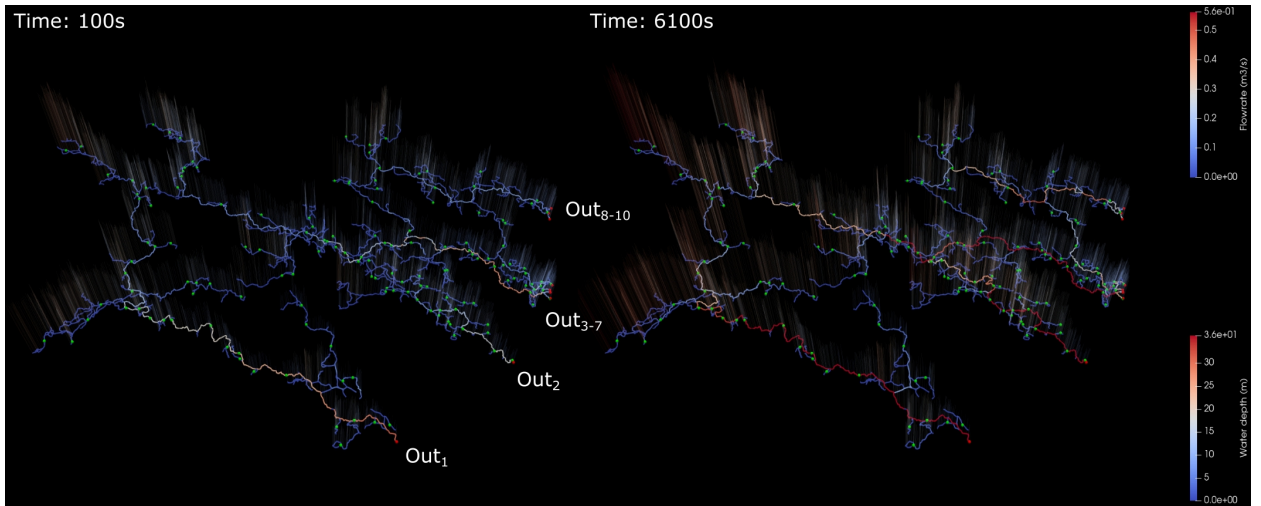


Figure 10: Flow results of the Ox Bel Ha cave network recharge scenario. Conduit colors represent flow rates and vertical lines the nodal water depths. The left figure shows the system close to steady-state conditions when the injection pulse starts ramping up (see Fig. 11, upper left). Green spheres indicate the sinkhole locations, red spheres the outlets. The right figure shows the system at maximum outlet discharge, which occurs at about 50 min after the maximum peak of the recharge signal.

connected to outlet 2 forms a trough that can accommodate larger water volumes during the recharge event, and hence is activated with a slight delay.

These processes can also be observed in Fig. 11 which shows the discharge, the fraction of pressurized conduits, the fraction of turbulent conduits and the ratio of main branches to total branches. In terms of outflow volume the branch connected to outlet 3-7 receives the highest amount of discharge due to its central location and hence highest contributing upstream conduit volume, while outlet 8-10 receive the lowest amount of recharge from the upstream network. The activation of the previously discussed trough area connected to outlet 2 can be observed in the graph showing the fraction of turbulent conduits (upper right). These range from about 50 % under steady-state conditions to a maximum of about 70 % at the maximum injection rate after 1 h. A second maximum after about 2 h can be attributed to the filling of the trough area connected to outlet 2 and furthermore the delayed filling of the northeastern branches.

The whole network is nearly fully pressurized over the whole simulation period. Only about 0.25 % of conduits located close to the merging point of main branches connected to outlet 2 and outlet 3-7 are in a free-surface flow mode at steady-state (lower left). Here a local maximum of the conduit base heights is observed while conduit elevations drop towards the northeastern coastline and the northwestern parts. In order to quantify the flow focusing properties of the network we compute the time-dependent ratio of main branch volume to total conduit volume based on the percentile of flow rates (lower right graph). The network exhibits a very strong degree of flow focusing. The top 5 % of conduits with highest flow rates make up partially less than 5 % of the total conduit volume, and hence form dominant pathways.

5. Conclusion and future directions

In this paper we have developed a new Python-based code for the simulation of highly dynamic flows in complex karst conduit networks via the dynamic wave equation. openKARST is written in an efficient vectorized form and provides all basic functionalities for the systematic investigation of the impact of network geometry and heterogeneity on the flow dynamics in karst networks. The code simulates free-surface flow and dynamic transitions to fully-pressurized conditions both under laminar and turbulent conditions governed by the Darcy-Weisbach and Manning equation using a continuous Churchill friction factor formulation. The code is easy to use and comes with a variety of examples and online documentation. It has been carefully verified and validated for steady-state and transient flow dynamics. Finally, we have used the code to solve for flow in the Ox Bel Ha cave network system, and assess the influence of network topology and geometry on transient recharge and integrated discharge dynamics.

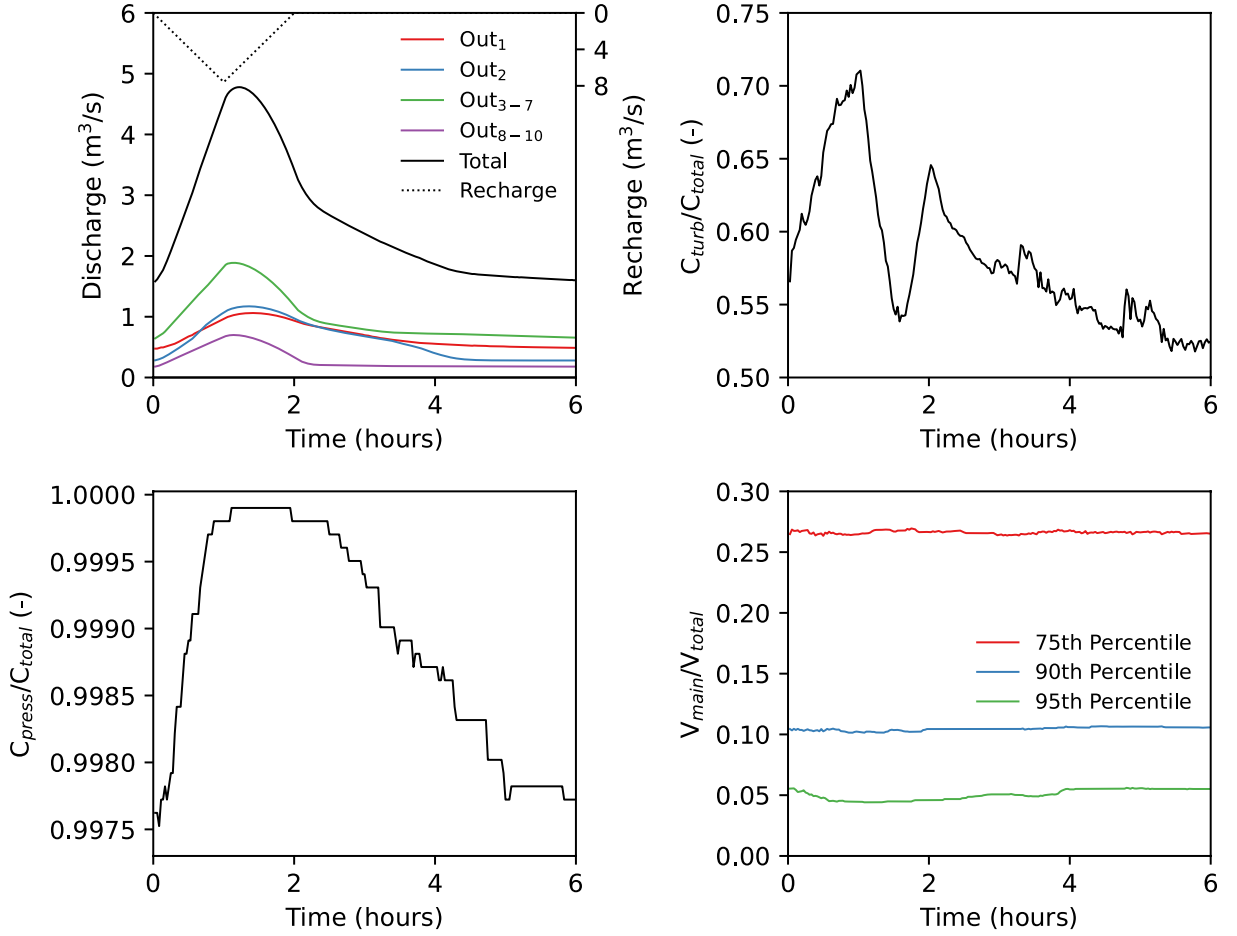


Figure 11: (Upper left) Discharge at various outflow nodes along the eastern coastline (see Fig. 10), where outflows for close nodes have been combined. The recharge signal (right y-axis) peaks at 1 h with a maximum of $7.59 \text{ m}^3/\text{s}$, i.e., the total recharge applied to all 152 sinkholes. (Lower left) Fraction of conduits that are in a pressurized state. (Upper right) Fraction of conduits that exhibit turbulent flow. (Lower right) Volume ratio of the main pathways identified based on the percentile of flow rates, indicating a high flow concentration in the network.

Future directions encompass the implementation of solute transport on different levels of complexity via the advection-dispersion equation, random walk particle tracking, and time-domain random walks (Noetinger et al., 2016), improved geometry descriptors based on cave surveys to replace circular geometries (Collon et al., 2017), and coupling of flow and transport to the porous matrix systems via the source-sink terms in the continuity and momentum equations.

Furthermore, a key feature of flow in karst conduits is the complex internal geometry of the latter and its impact on conduit scale flow. openKARST's modular structure allows to implement alternative relations for the friction slope adapted to large roughness (Huang et al., 2013; De Maio et al., 2023).

Acknowledgements

The authors acknowledge funding by the European Union (ERC, KARST, 101071836). Views and opinions expressed are however those of the authors only and do not necessarily reflect those of the European Union or the European Research Council Executive Agency. Neither the European Union nor the granting authority can be held responsible for them. We thank James G. Coke for spending the time preparing and sharing with us the survey data, the GEO (Grupo de Exploración Ox Bel Ha), the MCEP (Mexico Cave Exploration Project), the QRSS (Quintana Roo

Speleological Survey), the CINDAQ (El Centro Investigador del Sistema Acuífero de Quintana Roo), and all the cave surveyor who explored and mapped the cave over the years.

Code availability section

Name of the code/library: openKARST

Contact: Jannes Kordilla, kordilla@googlemail.com

Hardware requirements: 64 bit

Program language: Python 3

Software required: Windows, UNIX/Linux, macOS

Program size: 9.34 MB (including example data)

The source code and analytical solutions are available for download at: <https://doi.org/10.5281/zenodo.13961334>

License type: GPL

A. Derivation of Equation (4)

In order to derive Eq. (4), we combine the continuity equation (65) and (3) as follows. First expand the inertia term in Eq. (3) as

$$\frac{\partial}{\partial x} \left(\frac{Q^2}{A} \right) = 2 \frac{Q}{A} \frac{\partial Q}{\partial x} - \frac{Q^2}{A^2} \frac{\partial A}{\partial x}. \quad (63)$$

Using the definition $Q = vA$, we can write this expression as

$$\frac{\partial}{\partial x} \left(\frac{Q^2}{A} \right) = 2v \frac{\partial Q}{\partial x} - v^2 \frac{\partial A}{\partial x}. \quad (64)$$

Per the continuity equation (65), the spatial derivative of Q is

$$\frac{\partial Q}{\partial x} = -\frac{\partial A}{\partial t} + q. \quad (65)$$

Thus, we obtain for the inertia term

$$\frac{\partial}{\partial x} \left(\frac{Q^2}{A} \right) = -2v \left(\frac{\partial A}{\partial t} - q \right) - v^2 \frac{\partial A}{\partial x}. \quad (66)$$

Inserting this expression for the inertia term in Eq. (3) gives Eq. (4).

CRedit authorship contribution statement

Jannes Kordilla: Conceptualization, Methodology, Software, Validation, Formal analysis, Investigation, Writing - Original Draft, Visualization. **Marco Dentz:** Conceptualization, Methodology, Writing - Original Draft, Funding acquisition. **Juan J. Hidalgo:** Conceptualization, Methodology, Writing - Original Draft.

References

- Bakalowicz, M., 2015. Karst and karst groundwater resources in the Mediterranean. *Environmental Earth Sciences* 74, 5–14. URL: <http://dx.doi.org/10.1007/s12665-015-4239-4>, doi:10.1007/s12665-015-4239-4.
- Berre, I., Doster, F., Keilegavlen, E., 2019. Flow in fractured porous media: A review of conceptual models and discretization approaches. *Transport in Porous Media* 130, 215–236.
- Bresinsky, L., Kordilla, J., Engelhardt, I., Livshitz, Y., Service, H., Authority, I.W., St, I., 2023. Variably saturated dual-continuum flow modeling to assess distributed infiltration and vadose storage dynamics of a karst aquifer - The Western Mountain Aquifer in Israel and the West. *Journal of Hydrology X* 18, 100143. URL: <https://doi.org/10.1016/j.hydroa.2022.100143>, doi:10.1016/j.hydroa.2022.100143.
- Campbell, C.W., Sullivan, S.M., 2002. Simulating time-varying cave flow and water levels using the storm water management model. *Engineering Geology* 65, 133–139.

- Chen, Z., Auler, A.S., Bakalowicz, M., Drew, D., Griger, F., Hartmann, J., Jiang, G., Moosdorf, N., Richts, A., Stevanovic, Z., Veni, G., Goldscheider, N., 2017. The World Karst Aquifer Mapping project: concept, mapping procedure and map of Europe. *Hydrogeology Journal* 25, 771–785. doi:10.1007/s10040-016-1519-3.
- Chen, Z., Goldscheider, N., 2014. Modeling spatially and temporally varied hydraulic behavior of a folded karst system with dominant conduit drainage at catchment scale, hochifen–gottesacker, alps. *Journal of Hydrology* 514, 41–52.
- Chen, Z., Hartmann, A., Wagener, T., Goldscheider, N., 2018. Dynamics of water fluxes and storages in an Alpine karst catchment under current and potential future climate conditions. *Hydrology and Earth System Sciences* 22, 3807–3823. doi:10.5194/hess-22-3807-2018.
- Chow, V.T., 1959. Open channel hydraulics. McGraw-Hill, New York.
- Churchill, S.W., 1977. Friction-factor equation spans all fluid-flow regimes. *Chemical Engineering (New York)* 84, 91–92.
- Colebrook, C.F., White, C.M., 1937. Experiments with fluid friction in roughened pipes. *Proceedings of the Royal Society of London. Series A - Mathematical and Physical Sciences* 161, 367–381. doi:10.1098/rspa.1937.0150.
- Collon, P., Bernasconi, D., Vuilleumier, C., Renard, P., 2017. Statistical metrics for the characterization of karst network geometry and topology. *Geomorphology* 283, 122–142.
- Cornaton, F., Perrochet, P., 2002. Analytical 1d dual-porosity equivalent solutions to 3d discrete single-continuum models. application to karstic spring hydrograph modelling. *Journal of Hydrology* 262, 165–176.
- Cunge, J., Wegner, M., 1966. Numerical integration of barré de saint-venant’s flow equations by means of an implicit scheme of finite differences. applications in the case of alternately free and pressurized flow in a tunnel. *La Houille Blanche* 22, 33–39.
- De Maio, M., Latini, B., Nasuti, F., Pirozzoli, S., 2023. Direct numerical simulation of turbulent flow in pipes with realistic large roughness at the wall. *Journal of Fluid Mechanics* 974, A40.
- Delestre, O., 2010. Simulation du ruissellement d’eau de pluie sur des surfaces agricoles. Ph.D. thesis. Mathématiques [math]. Université d’Orléans. URL: <https://theses.hal.science/tel-00531377v1>.
- Delestre, O., Lucas, C., Ksinant, P.A., Darboux, F., Laguerre, C., Ngoc, T., Vo, T., James, F., Cordier, S., Delestre, O., Lucas, C., Ksinant, P.A., Darboux, F., Laguerre, C., Vo, T.N.T., James, F., Cordier, S., Dieudonné, J.A., 2013. SWASHES: a compilation of Shallow Water Analytic Solutions for Hydraulic and Environmental Studies Christian Laguerre, et al. SWASHES: a compilation of Shallow Water Analytic Solutions for Hydraulic and Environmental Studies SWASHES: a compilation of Sh. *International Journal for Numerical Methods in Fluids* 72, 269–300. URL: <http://www.univ-orleans.fr/mapmo/soft/SWASHES>, doi:10.1002/flid.3741Åř.
- Devos, F., Fortin, J., Le Maillot, C., Meacham, S., Taylor, D.P., 2023. CINDAQ 2022 Annual Report. Technical Report. El Centro Investigador del Sistema Acuífero de Quintana Roo A.C.(CINDAQ).
- Ersoy, M., Lakkis, O., Townsend, P., 2020. A Saint-Venant Model for Overland Flows with Precipitation and Recharge. *Mathematical and Computational Applications* 26, 1. URL: <https://www.mdpi.com/2297-8747/26/1/1>, doi:10.3390/mca26010001.
- Fread, D., Jin, M., Lewis, J.M., 1996. An lpi numerical implicit solution for unsteady mixed-flow simulation, in: *North American Water and Environment Congress & Destructive Water*, ASCE. pp. 322–327.
- Hartmann, A., Goldscheider, N., Wagener, T., Lange, J., Weiler, M., 2014. Karst water resources in a changing world: Review of hydrological modeling approaches. *Reviews of Geophysics* 52, 218–242.
- Hayami, S., 1951. On the propagation of flood waves. *Bulletins-Disaster Prevention Research Institute, Kyoto University* 1, 1–16.
- Huang, K., Wan, J., Chen, C., Li, Y., Mao, D., Zhang, M., 2013. Experimental investigation on friction factor in pipes with large roughness. *Experimental Thermal and Fluid Science* 50, 147–153.
- Jeannin, P.Y., 2001. Modeling flow in phreatic and epiphreatic karst conduits in the h  loch cave (muotatal, switzerland). *Water Resources Research* 37, 191–200.
- Jourde, H., Wang, X., 2023. Advances, challenges and perspective in modelling the functioning of karst systems: a review. *Environmental Earth Sciences* 82, 396.
- Kiraly, L., 1975. Rapport sur l’  tat actuel des connaissances dans le domaine des caract  res physiques des roches karstiques, in: *Hydrogeology of karstic terrains*, pp. 53–67.
- Kordilla, J., Sauter, M., Reimann, T., Geyer, T., 2012. Simulation of saturated and unsaturated flow in karst systems at catchment scale using a double continuum approach. *Hydrology and Earth System Sciences* 16, 3909–3923. doi:10.5194/hess-16-3909-2012.
- Kov  cs, A., Sauter, M., 2014. Modelling karst hydrodynamics, in: *Methods in karst hydrogeology*. CRC Press, pp. 201–222.
- Kresic, N., Panday, S., 2018. Numerical groundwater modelling in karst. *Geological Society, London, Special Publications* 466, 319–330.
- Langtangen, H.P., Linge, S., 2017. Finite difference computing with PDEs: a modern software approach. Springer Nature.
- Larocque, M., Banton, O., Ackerer, P., Razack, M., 1999. Determining karst transmissivities with inverse modeling and an equivalent porous media. *Groundwater* 37, 897–903.
- Maqueda, A., Renard, P., Filipponi, M., 2023. Karst conduit size distribution evolution using speleogenesis modelling. *Environmental Earth Sciences* 82, 1–16. URL: <https://doi.org/10.1007/s12665-023-11035-6>, doi:10.1007/s12665-023-11035-6.
- Neuman, S.P., 2005. Trends, prospects and challenges in quantifying flow and transport through fractured rocks. *Hydrogeology Journal* 13, 124–147. doi:10.1007/s10040-004-0397-2.
- Noetinger, B., Roubinet, D., Russian, A., Le Borgne, T., Delay, F., Dentz, M., De Dreuzey, J.R., Gouze, P., 2016. Random walk methods for modeling hydrodynamic transport in porous and fractured media from pore to reservoir scale. *Transport in Porous Media* , 1–41.
- Panday, S., Langevin, C.D., Niswonger, R.G., Ibaraki, M., Hughes, J.D., 2013. MODFLOW–USG version 1: An unstructured grid version of MODFLOW for simulating groundwater flow and tightly coupled processes using a control volume finite-difference formulation. Technical Report. US Geological Survey.
- Peterson, E.W., Wicks, C.M., 2006. Assessing the importance of conduit geometry and physical parameters in karst systems using the storm water management model (swmm). *Journal of hydrology* 329, 294–305.
- Preissmann, A., 1961. Propagation of transitory waves in channels and rivers, in: *Proc., 1st Congress of French Association for Computation, AFCAL, Grenoble, France*. pp. 433–442.

- Reimann, T., Geyer, T., Shoemaker, W.B., Liedl, R., Sauter, M., 2011. Effects of dynamically variable saturation and matrix-conduit coupling of flow in karst aquifers. *Water Resources Research* 47, 1–19. doi:10.1029/2011WR010446.
- Rossman, L.A., Huber, W.C., 2017. Storm Water Management Model Reference Manual: Volume II – Hydraulics. Technical Report. U.S. Environmental Protection Agency, National Risk Management Laboratory. Cincinnati.
- Saint-Venant, A.D., 1871. Theorie du mouvement non permanent des eaux, avec application aux crues des rivières et à l'introduction de marées dans leurs lits. *Comptes rendus des séances de l'Académie des Sciences* 36, 174–154.
- Scanlon, B.R., Mace, R.E., Barrett, M.E., Smith, B., 2003. Can we simulate regional groundwater flow in a karst system using equivalent porous media models? Case study, Barton Springs Edwards aquifer, USA. *Journal of Hydrology* 276, 137–158. doi:10.1016/S0022-1694(03)00064-7.
- Schmidt, S., Geyer, T., Guttman, J., Marei, A., Ries, F., Sauter, M., 2014. Characterisation and modelling of conduit restricted karst aquifers - Example of the Auja spring, Jordan Valley. *Journal of Hydrology* 511, 750–763. URL: <http://dx.doi.org/10.1016/j.jhydrol.2014.02.019>, doi:10.1016/j.jhydrol.2014.02.019.
- Shigorina, E., Rüdiger, F., Tartakovsky, A.M., Sauter, M., Kordilla, J., 2021. Multiscale Smoothed Particle Hydrodynamics Model Development for Simulating Preferential Flow Dynamics in Fractured Porous Media. *Water Resources Research* 57. doi:10.1029/2020WR027323.
- Shoemaker, W., Kuniansky, E., Birk, S., Bauer, S., Swain, E., 2007. Documentation of a Conduit Flow Process (CFP) for MODFLOW-2005, in: *Techniques and Methods Book 6*. chapter A24. doi:doi.org/10.3133/tm6A24.
- Shoemaker, W.B., Cunningham, K.J., Kuniansky, E.L., Dixon, J., 2008. Effects of turbulence on hydraulic heads and parameter sensitivities in preferential groundwater flow layers. *Water Resources Research* 44, 1–11. doi:10.1029/2007WR006601.
- Sjöberg, A., 1982. Sewer network models DAGVL-A and DAGVL-DIFF, in: Yen, B.C. (Ed.), *Urban stormwater hydraulics and hydrology*. Water Resource Publications, Littleton, CO, pp. 127–136.
- Swamee, P.K., Jain, A.K., 1976. Explicit equations for pipe-flow problems. *Journal of the hydraulics division* 102, 657–664.